Nanoscale Heterogeneity in $CsPbBr_3$ and $CsPbBr_3$:KI Perovskite Films Revealed by Cathodoluminescence Hyperspectral Imaging

Lethy Krishnan Jagadamma[1+], Paul R. Edwards[2+], Robert W. Martin[2], Arvydas Ruseckas[1], Ifor D. W. Samuel[1*]*

Dr. L.K. Jagadamma, Dr. A. Ruseckas, Prof. I.D.W. Samuel
Organic Semiconductor Centre, SUPA, School of Physics & Astronomy, North Haugh, St Andrews, KY16 9SS, United Kingdom

Dr. P.R. Edwards, Prof. R.W. Martin
Department of Physics, SUPA, University of Strathclyde, 107 Rottenrow, Glasgow
G4 0NG, United Kingdom

E-mail: paul.edwards@strath.ac.uk & idws@st-andrews.ac.uk
[+] These authors contributed equally

Keywords: halide perovskites, grain-to-grain inhomogeneity, gradient in bandgap, local strain, local phase segregation

Abstract

The nanoscale morphology of solar cell materials strongly affects their performance. We report direct evidence for the existence of multiple length scales of heterogeneity in halide perovskites such as $CsPbBr_3$ and $CsPbBr_3$:KI. Contrary to the general notion of two distinct phases, our study suggests the presence of multiple phases in mixed halide perovskites. Highly spatially resolved (≈50 nm) cathodoluminescence maps reveal that the length scale of heterogeneity is composition dependent: smaller (≈ 200 nm) for $CsPbBr_3$, and larger (≈500–1000 nm) for $CsPbBr_3$:KI. Moreover, these nano-/micro-scale heterogeneities exist both laterally and vertically in mixed halides and correlate with high densities of carrier traps and fast trap-assisted recombination. The observed heterogeneities also lead to reduced power conversion efficiency of solar cells, higher hysteresis loss, and faster degradation. These insights argue for advanced nanoscale characterization of halide perovskites to guide reduction of heterogeneity and so improve device performance and stability.

1. Introduction

Non-radiative recombination losses in the halide perovskite solar cells reduce their efficiency below the Shockley-Queisser limit and accelerate degradation.[1-3] Recent studies suggest that these losses are linked to the multiple length scales of heterogeneity in the perovskite photoactive layers.[4] These heterogeneities range across sub-grain (<100 nm), grain-to-grain (0.1–10 µm) and long-range (>10 µm) scales, arising from non-uniform chemical composition or residual strain.[4-5] Strain accelerates the degradation of halide perovskite films by reducing the activation energy for ion migration and cause non-radiative losses.[6-8] The polycrystalline nature and simple solution-based fabrication of halide perovskites cause localised stoichiometric deviation and extrinsic defects, such as grain boundaries.[9] These nanoscale heterogeneities dictate the local bandgap, affect charge transport, and govern the optoelectronic properties. The distribution of non-radiative recombination across the sample surface has previously been investigated using confocal photoluminescence (PL) microscopy and very recently using photoemission electron microscopy.[10-14] However, these measurements mostly probed the samples' near-surface region and local variations in PL *intensity* only, whereas the output performance of halide perovskite optoelectronic devices is sensitive to heterogeneity at all length scales and directions (i.e. both lateral and vertical).[4] Vertical transport of charge carriers is central to the performance of solar cells, photodetectors and LEDs, and control of vertical heterogeneity in composition and light emission is needed to avoid unbalanced electronic transport rates, charge collection and trapping issues. Highly spatially resolved luminescence data has been reported for hybrid perovskite films using monochromatic and panchromatic cathodoluminescence (CL) mapping.[15-19] Depth-resolved CL emission intensity maps have revealed a lateral and vertical heterogeneity in the distribution of non-radiative recombination centres. However, these reports did not reveal any heterogeneity in peak emission energy which may arise from local composition variation or local strain.

$CsPbBr_3$ (bandgap E_g 2.3 eV), is a promising material for LEDs,[20] lasers,[21] Si/perovskite tandems,[22] transparent solar cells,[23] and indoor photovoltaics,[24] and possesses enhanced stability to heat, oxygen and moisture compared to the hybrid $CH_3NH_3PbX_3$.[25-28] Compared to iodides, wide bandgap lead bromide perovskites show significantly higher open circuit voltage (V_{OC}) deficits,[29] with > 0.7 V reported for even for the best $CsPbBr_3$ solar cells[25]. Metal ion incorporation is a promising approach to enhance the stability and performance of perovskite electronic devices.[30-33] Incorporation of potassium iodide (KI) into $CH_3NH_3PbI_3$ and $Cs_{0.06}FA_{0.79}MA_{0.15}Pb(I_{0.85}Br_{0.15})_3$ has been shown to mitigate non-radiative losses (hence improving V_{OC} and fill-factor FF) and photo-induced halide ion-migration (Br^-).[34-35] Despite these beneficial effects of KI, mixed results have been reported regarding the surface vs bulk occupancy of K^+ and I^- ions, Fermi level (E_F) shifts due to doping, influence on phase segregation and composition homogeneity. Previously halide phase segregation at grain boundaries and *in situ* scanning electron CL imaging to exploit the nanoscale structural transformation in $CsPbIBr_2$ have been reported[36-37]; however the length scale of these heterogeneities, their spatial distribution and correlation with optoelectronic device performance remain open questions.

In the present study, we unravel the nanoscale heterogeneity in the material properties of $CsPbBr_3$ and $CsPbBr_3$:KI thin films and their impact on the optoelectronic device performance. Although the cathodoluminescence technique is known widely and has previously reported for halide perovskites,[38] our study is the first to exploit the full potential of the hyperspectral imaging mode to reveal how material properties such as bandgap, phase segregation and defects are spatially distributed with nanometer scale spatial resolution (≈50 nm). By combining features of both spectroscopy and microscopy, cathodoluminescence hyperspectral imaging (CLHSI) allows simultaneous collection of spatially and spectrally resolved data, with high lateral spatial resolution down to ≈ 20 nm.[39-41] We exploit the full potential of the three-dimensional CLHSI data cube (luminescence intensity as a function of two spatial and one spectral dimension) using the spectrum-processing operations of peak fitting. By selecting suitable electron beam conditions, such nanoscale heterogeneity in light emission intensity, emission energy, and full-width at half-maximum (FWHM) is mapped for $CsPbBr_3$ and KI-incorporated $CsPbBr_3$ films. Our findings provide direct evidence for nanoscale local heterogeneity in halide perovskites, and that this correlates with the macroscopic optoelectronic properties.

2. Results and Discussion

2.1. Microstructural and optoelectronic properties

In this study we have selected low temperature (100 °C) and single step processed $CsPbBr_3$ and $CsPbBr_3$:KI films for CL hyperspectral mapping. Previous studies[20, 42-43] have shown that $CsPbBr_3$ films prepared under these conditions have good light emission properties which is crucial for getting high signal-to-noise ratio CL hyperspectral mapping. Even though the wide bandgap of 2.3 eV is not ideal for outdoor solar cells applications, this bandgap is in the suitable range for indoor[44] and transparent photovoltaics[45] (~ 2 eV), and thus the obtained results are significant for various $CsPbBr_3$ based optoelectronic devices including photovoltaics.

Optical properties of the $CsPbBr_3$ and $CsPbBr_3$:KI films obtained using PL spectroscopy and UV-visible absorption measurements are shown in **Figure 1(a).** The optoelectronic properties were investigated for CsBr:KI weight ratios of 1:0 and 1:0.1, as these match the previously reported KI incorporation in hybrid perovskites.[34] Optical properties of all the prepared films are shown in Supplementary Information (SI) (**Figure S1**). Figure 1a shows the symmetric PL emission [(Figure S1(c)] for $CsPbBr_3$ films at 532 nm. With KI incorporation this PL peak broadens [15 nm vs 20 nm, shown in Figure S1(b)] and redshifts to 538 nm. The UV-vis absorption spectra of the $CsPbBr_3$:KI films also show a redshift of ≈6 nm in the absorption edge (bandgap decreasing from 2.33 to 2.30 eV). These redshifts imply that the iodide ion does not remain tightly bound to K^+ at the surface of the perovskite but enters the structure, affects bulk related properties, and results in the formation of a Caesium-lead mixed iodide-bromide composition. A similar effect of bandgap modification of $CsPbBr_3$ due to KI incorporation has been previously reported by Yousra *et al*.[46] Broader PL emission has been previously reported for mixed halides compared to pure halide perovskites.[47-48]

To understand how the KI incorporation influences the electronic band structure of the $CsPbBr_3$, the work function and valence band energy of the films were measured [**Figure 1(b) &** (**Figure S2**)]. The position of E_F with respect to the valence band suggests the *p*-type nature of the $CsPbBr_3$ films and agrees with previous reports.[49-51] The *p*-type conductivity is attributed to either Pb^{2+} vacancies or halide (Br^-) interstitials.[30, 52-53] The KI incorporation changes the electronic band structure of $CsPbBr_3$ with its valence band energy shifting towards the vacuum level and E_F being close to mid-gap showing the intrinsic nature of the $CsPbBr_3$:KI films. The slightly shallower ionization potential indicates the formation of the mixed iodide-bromide material due to the mixing of $4p^6$ and $5p^6$ orbitals from iodine and bromine atoms, respectively. This observation supports the redshift in absorption band edge and PL peak as discussed above [Figure 1(a)]. The intrinsic nature of the $CsPbBr_3$:KI films indicates that K^+ ions suppress Br^- ion migration and interstitial halide formation as reported by Adbi-Jalebi *et al*. for KI-incorporated $CH_3NH_3PbI_3$ films.[34]

The structural and morphological properties of the films were studied using X-ray diffraction (XRD) [**Figure 1(c)**] and scanning electron microscopy (SEM) measurements [**Figure 1(d)**]. The XRD pattern of $CsPbBr_3$ shows distinct peaks at 2θ values of 15.2°, 21.6°, 30.4°, 30.7° and 35.2° which are assigned to (010), (110), (002), (020) and (120) planes of the tetragonal phase,[55] respectively, and reveal the polycrystalline nature of the $CsPbBr_3$. With KI incorporation, this polycrystalline nature is preserved but the diffraction peaks broaden and the relative intensity of peaks at 21.6°, 30.4° and 35.2° is modified. This shows that KI incorporation modifies both the domain size and their preferential orientation. Previous studies of KBr doping in $CsPbBr_3$ have shown increased X-ray diffraction intensity and lattice contraction due to K^+ (1.38 Å) replacing the Cs^+ (1.67 Å), shifting the diffraction angles to higher values.[32-33, 46] In contrast to this, our study shows that introduction of KI shifts the main X-ray diffraction peaks of $CsPbBr_3$ [corresponding to (010), (110) and (020) planes] towards the lower diffraction angles (15.2° *vs* 15.1°, 30.7° *vs* 30.6°, 21.6° *vs* 21.5°). These shifts to lower diffraction angles are an indication of preferential incorporation of the hetero-anion I^- (2.20 Å) replacing the Br^- (1.96 Å) in the $CsPbBr_3$ lattice and/or suppressing or compensating any effects due to K^+ incorporation replacing the Cs^+ (even if it occurs).

The surface morphology of the $CsPbBr_3$ and $CsPbBr_3$:KI films is further characterised using SEM images [Figure 1(d)], in which grain-*like* and grain-boundary-*like* features are visible for both films. These terms are used with caution here, as there is wide debate regarding grain and grain boundaries in the hybrid perovskites.[56-57] Recently Rothmann *et al*[58] have suggested that grain boundaries can be benign by observing highly crystalline and undisturbed perovskite structure across the grain boundaries in $FAPbI_3$ and $MAPbI_3$ using atomic resolution imaging techniques. The SEM image of $CsPbBr_3$ shows voids with size and density of approximately 50 nm and 2 μm^{-2}, respectively. Incomplete surface coverage of single-step processed $CsPbBr_3$ has previously been reported[42-43] The incorporation of KI alters the morphology, with improved surface coverage and comparable domain sizes but a different growth pattern and highly compact domains. This is in contrast to the previously reported effect of increased domain size for $CsPbBr_3$ grains due to KBr doping.[33] A similar increased grain size has also been reported by Nam et al for $CsPbI_2Br$ grains due to K^+.[32] This lack of increased grain size in $CsPbBr_3$ due to KI incorporation again supports the inference that effective replacement of Cs^+ ions by K^+ in $CsPbBr_3$ is suppressed due to the presence of hetero-anions of I^-. A related observation of increased surface coverage in $CsPbBr_3$ films with ZnO nanoparticle incorporation implies that KI modifies the nucleation properties of $CsPbBr_3$

films.[43]The presence of KI in the $CsPbBr_3$ film is verified by Energy dispersive X-ray spectroscopy (EDS) as shown in Figure S2(c) and (d).

2.2 Depth resolved CL

In CL spectroscopy, depth resolved light emission properties of thin film samples can be obtained by varying the electron beam acceleration voltage.[59] To probe any heterogeneity in light emission across sample thickness, CL spectra were recorded for $CsPbBr_3$ and $CsPbBr_3$:KI films for electron beam voltages of 2 kV and 4 kV. Estimates of the CL generation depth under these conditions are obtained using Monte Carlo simulations[60] [**Figure 2(a)**]. For a 2 kV beam the CL emission mainly originates from the first 50 nm of material, while at 4 kV up to ≈130 nm is probed. The corresponding depth-resolved CL spectra are shown in **Figure 2(b)**. The CL spectra from $CsPbBr_3$ at 2 kV and 4 kV, with the electron beam current held at ≈1 nA, show a similar profile with peak emission at 524 nm in both cases and full widths at half maximum (FWHM) of 17 nm. The observation is different for the $CsPbBr_3$:KI sample, which shows a distinct *depth-dependent peak shift and peak broadening*. At 2 kV the peak is centered at 528 nm (17 nm FWHM), red shifting to 538 nm (22 nm FWHM) at 4 kV. This redshift and broadening of the CL emission with increasing depth point to vertical compositional heterogeneity for the $CsPbBr_3$:KI, with an iodide-rich mixed halide occupying the bulk. Any effect of beam damage is excluded here as the CL emission signal was stable over the measurement timescale (see SI for validation of this). Similarly, self-absorption can be eliminated as the cause of the redshift, as the FWHM is *broader* for the CL excited from deeper in the sample.[61].

Even though the smaller size of the K^+ ions should allow them to substitute Cs^+ ions, previous studies show that K^+ is too small to occupy the Cs^+ site while preserving the $PbBr_6$ octahedral unit.[32, 34, 46] Moreover, Cs^+ replacement by K^+ would lead to lattice contraction and hence a blueshift in the bandgap. Since, in $CsPbBr_3$:KI, a redshift in CL emission is observed from the bulk compared to the surface, the K^+ ions might be occupying sites near the grain boundaries. Any blueshift in bandgap due to a mixed cation $Cs_{1-x}K_x$ (even if formed in small amounts) might be dominated by the emission from the mixed bromide-iodide in the bulk.

2.3 CL hyperspectral imaging

To understand how this vertical CL heterogeneity in $CsPbBr_3$:KI relates to the lateral heterogeneity, CL hyperspectral maps were obtained at the same two beam voltages. The 3D nature of the CLHSI data cubes makes it possible to extract the spatial distribution of spectral position, intensity, and width of one or more CL peaks in a single scan. The 2D maps in **Figure 2(c–f)** show how the emission properties of the $CsPbBr_3$ and $CsPbBr_3$:KI thin films differ across the scanned area of 2×2 µm for a 2 kV electron beam (the probed region is approximately 50 nm wide and deep, before carrier diffusion). These maps were obtained by Gaussian peak fitting to each spectrum in the hyperspectral image;[41] details of this procedure is given in the SI. Corresponding SEM images are given in **Figure S3**.

Although the emission intensity [**Figure 2(c,e)**] appears more uniform for the $CsPbBr_3$ film compared to $CsPbBr_3$:KI, histogram plots of pixel frequency vs peak intensity [**Figure S4(a)**] show little difference in the intensity distributions. A comparison of the CL peak energy maps [**Figure 2(d,f)**] reveals interesting spatial distribution properties. The $CsPbBr_3$ peak energy is plotted on a 25 meV scale and is largely homogeneous with an average domain size of emission features ≈200 nm. However, for $CsPbBr_3$:KI, the overall emission energy is redshifted, the scale is extended to 40 meV and highly localized emissive regions with domain size ≈0.5µm are observed. The overall redshift in emission energy for $CsPbBr_3$:KI suggests the formation of mixed halides $Cs_{1-x}K_xPbBr_{3-y}I_y$ with a smaller bandgap than $CsPbBr_3$ and agrees with the UV-vis absorption and PL measurements [Figures 1(a) and 2(b)]. This redshift is seen quantitatively in histogram plots of pixel frequency vs CL peak energy [Figure S4(b)]. The small variation in emission energy (≈20 meV) observed for the $CsPbBr_3$ may be due to small compositional fluctuations, strain or defects in the film.[5, 26, 56] The larger energy variation seen in $CsPbBr_3$:KI can be attributed to compositional heterogeneity arising from phase segregation in mixed iodide-bromide compositions. The corresponding FWHM maps and their histograms [**Figure S5(a)-(c)**] show that CL emission from $CsPbBr_3$ is slightly broader (≈ 95 meV) compared to that from $CsPbBr_3$:KI (≈ 90 meV). This could be related to the differences in surface texture between the two samples.

CLHSI using a 4 kV beam increases the width and depth of the probed region to ≈130 nm. SEM images of the mapped area (2×2 µm) are shown in **Figure S6**. For $CsPbBr_3$, the peak energy map [**Figure 2(g)**] shows an overall variation in peak position of ≈20 meV across the mapped area, similar to what observed for a 2 kV beam (probing depth ≈50 nm). This implies that for $CsPbBr_3$, the CL emission energy has no depth dependence. Also, for most grains the outer regions are found to be blue shifted compared to the grain centre as supported by the peak energy map overlaid on the SE image [**Figure S7(a)**]. This blueshift may be due to slight compositional variations or local compressive strain arising from the misorientation of adjacent grains during growth.[5, 26, 56] Strain effects due to incomplete surface coverage (commonly seen in $CsPbBr_3$ films) also cannot be excluded.

In contrast, the peak energy map for $CsPbBr_3$:KI at 4 kV [Figure 2(h)] shows the CL emission to be depth dependent. Compared to the 2 kV map, [Figure 2(f)], the 4 kV map exhibits an overall redshift, larger localised emission energy domains (≈0.7–1.0 µm) and greater spread in peak energy (≈80 meV). These observations suggest that in $CsPbBr_3$:KI, the iodide content increases with depth, and that there is greater lateral composition heterogeneity further away from the surface region. The corresponding overlaid peak energy map and SE image are shown in Figure S6(b) and S7(b).

The CL intensity map for $CsPbBr_3$ [**Figure 3(a)**] shows intensity variations both grain-grain and within grains. In general, the darker regions correspond to areas in the proximity of grain boundaries, as supported by the overlaid CL intensity map and topographic image [**Figure 3(b)**]. Local strain can also account for the less intense emission from these boundary regions.[1, 7] Applying the peak fitting procedure to the 4kV CL hyperspectral maps from $CsPbBr_3$:KI reveals pixel-to-pixel variations in intensity and the appearance of multiple peaks. Since three distinct emission peaks were visible, the CL hyperspectral data set was fitted using three Gaussian functions. The peak energies were 2.32 eV, 2.24 eV and 2.15 eV and imply the existence of multiple mixed halide phases with different iodide concentrations. These different emission components were not detectable through PL or absorption measurements as presented in Figure 1(a). The intensity distribution maps for these three distinct emissions and representative fitted CL spectra are shown in **Figure 3 (c–h)**. The main emission peak is at 2.32 eV and corresponds to the main mixed bromide-iodide related emission from $CsPbBr_3$:KI (matching with the PL peak shown in Figure 1(a)). The lower energy peak at 2.24 eV and 2.15 eV can be attributed to emission from increasing content of iodide rich phases. The overlay of these intensity maps with topographic images is shown in **Figure 3(i–k)**. The corresponding SE image is shown in Figure S6(b). The 2.32 eV peak mainly comes from the grains, the maximum intensity is at the centre and reduces towards the boundaries. The 2.24 eV emission comes mostly from the grains, but small portion comes from areas between the grains. The 2.15 eV emission comes mainly from the regions between the grains and correspond to highest iodide-rich phase segregation.[37] The two peaks in Figure 3(h) may be due to emission from two different phases of $CsPbBr_{3-x}I_x$ with different iodide content. To obtain the peak energy map of $CsPbBr_3$:KI shown in Figure 2(h) only the main CL emission at 2.32 eV is allowed to vary in full Gaussian parameter space (intensity/energy/width), while the other two (noisier) peaks are fixed in energy and width. The existence of iodide rich phases near the grain boundary region is also supported by the FWHM map analysis as described in SI [**Figure S8**].

This observation of multiple phases in $CsPbBr_3$:KI contradicts the general notion that phase segregation in mixed halides occurs as a two-phase component.[62] Recently, Mahesh et al[63] predicted the possible existence of a continuum in iodide concentration or at least multiple phases in a halide segregated absorber. The consensus is that the presence of these low bandgap iodide-rich minority phases will 'pin' the open circuit voltage of the corresponding solar cells. Recently Nishida et al[8] have reported that heterogeneous composition can influence the stability of the hybrid perovskites. To understand how these nanoscale heterogeneities in $CsPbBr_3$ and multiple phases in $CsPbBr_3$:KI influence the functional devices, solar cells were fabricated using these and the performance parameters and shelf life stability are explored as discussed below.

2.4 Photovoltaic and photophysical properties

Solar cells were fabricated in the *n-i-p* configuration as shown in **Figure 4(a)**, with photovoltaic performance parameters listed in **Table S1**. The current-voltage characteristics of typical devices are shown in **Figure 4(b).** $CsPbBr_3$ based devices show higher power conversion efficiency (PCE) (1.16%) and lower hysteresis compared to $CsPbBr_3$:KI based devices (PCE 0.61%). In previous reports on $CsPbBr_3$ solar cells, the PCE mostly ranges from 3 to 6%[64] and the lower efficiency of our devices is due to the low processing temperature (100°C vs 300°C) and single step fabrication method used in the preparation of the active layers. These processing conditions were selected to favour high CL intensity, since $CsPbBr_3$ prepared under these conditions has shown to display good light emission properties.[20, 42-43] Hence the relatively low PCE of these films does not therefore imply poor quality. The larger spatial variations in CL intensity and photon energy in $CsPbBr_3$:KI [**Figure 2(f,h)**] and the presence of multiple CL bands [**Figure 3(c–e)**] are indicative of energy bandgap fluctuations which can trap the photogenerated charge carriers.[9, 65] Time-resolved photoluminescence is sensitive to the trap density in inorganic semiconductors and the PL decay measured at low excitation density is significantly faster in $CsPbBr_3$:KI than $CsPbBr_3$ [Fig 4(c)]. This indicates faster carrier trapping in $CsPbBr_3$:KI and a higher density of traps. Faster PL decay in $CsPbBr_3$:KI also occurs on a long-time scale where trapped and un-trapped carriers are in thermal equilibrium and trap-assisted recombination dominates. This is also consistent with more trapped carriers in $CsPbBr_3$:KI. Unbound K^+ ions on the perovskite surface might be contributing to this faster PL quenching in $CsPbBr_3$:KI. Previous studies have shown an increased lifetime of carriers in $CsPbBr_3$ due to KBr doping, credited to the dopant's passivation effect.[33, 46] However, Nam *et al*[32] have noted a decreased PL decay lifetime in $CsPbI_2Br$ films doped with KI. They attribute this to the residual potassium cations failing to occupy at the A- sites of the perovskite. The PL decay in $CsPbBr_3$ films on a long-time scale can be fitted with a time constant $\tau_{long} \approx 12$ ns. It is interesting to note that this decay time of 12 ns is longer than the PL decay lifetime in the range 1.5 to 5 ns reported earlier for pristine $CsPbBr_3$ and comparable to the lifetime of ~ 12-13 ns for $CsPbBr_3$ films with fewer bulk defects and good exciton confinement.[66-68] The longer PL decay lifetime in $CsPbBr_3$ films in our study indicates the high quality of the $CsPbBr_3$ films with less nanoscale heterogeneity and fewer bulk defects.

The faster trap-assisted recombination could be the reason for the lower J_{SC} values (Table S1) in $CsPbBr_3$:KI devices despite their absorption edge redshift [(Figure 1(a)]. The depth dependent compositional heterogeneity in $CsPbBr_3$:KI films can impede the vertical transport of the photogenerated charge carriers by adversely affecting the redistribution of the mobile ionic charge during the current-voltage scan, thus accounting for the higher hysteresis loss.[69] This vertical composition heterogeneity is detrimental to $CsPbBr_3$ based LEDs as well since this would result in spatial charge imbalance in electron and hole density limiting the quantum efficiency of the electroluminescence process[70]. It is interesting to note that, compared to $CsPbBr_3$, the existence of minority phases with lower bandgap does not limit the V_{OC} from the $CsPbBr_3$:KI, implying that the prevalence of these phases is below the threshold required for such losses [**Table S1 and Figure 4(b)**].

The shelf life stability of the $CsPbBr_3$ and $CsPbBr_3$:KI devices was tested over 20 days and is shown in Figure 4(d). For $CsPbBr_3$ devices, hysteresis slightly improves on ageing, whereas for $CsPbBr_3$:KI devices severe hysteresis loss persists. Analysis of the individual performances reveals that $CsPbBr_3$:KI devices suffer greater losses in V_{OC} and fill factor with ageing [**Table S2-S4, and Figure S9**].

For $CsPbBr_3$:KI films, the detailed CL hyperspectral mapping, and their optoelectronic and microstructural characterization all imply that the incorporation of a hetero-anion (of I^-) introduced through the potassium salt, KI, is effective in tuning the composition and optical properties of $CsPbBr_3$. Previous studies have shown the beneficial effect of KBr doping to $CsPbBr_3$, through lattice contraction, suppressed recombination losses, and increased phase stability.[32-33, 46] However, our study revealed lattice expansion, redshifted bandgap, increased recombination and higher hysteresis losses due to KI incorporation in $CsPbBr_3$. This implies that effect of I^- incorporation in replacing Br^- in $CsPbBr_3$ bulk dominates any influence due to K^+ replacing Cs^+.

3. Conclusion

In summary, we have revealed the presence of nanoscale heterogeneity in the material properties of the emerging optoelectronic materials of $CsPbBr_3$ and $CsPbBr_3$:KI. Our study demonstrates the existence of multiple phases with different bandgaps, with both lateral and vertical heterogeneity. The length scale of this heterogeneity is composition dependent: smaller for pure halide and larger for mixed halides. These heterogeneities in material properties cause trap-assisted recombination, adversely affecting photovoltaic devices based on $CsPbBr_3$:KI through lower power conversion efficiency and higher hysteresis loss. Our study further revealed that the role of K^+ ions in replacing Cs^+ at the A- site of the $CsPbBr_3$ perovskite is suppressed in the presence of hetero-anions of I^-, and that I^- preferentially replaces Br^- to form mixed halide perovskites. Our study strongly suggests that halide perovskite materials require detailed nanoscale characterisation of their heterogeneity, in order to guide approaches to mitigate localised stoichiometric deviations, and so realise their maximum optoelectronic functionality.

Supporting Information

Supporting information associated with this manuscript is attached as a separate file.

Competing interests:

The authors declare no competing interests

Acknowledgements

We are grateful for funding from the EPSRC under grant code EP/L017008/1. Dr. L. K. Jagadamma acknowledges support from a Marie Skłodowska-Curie Individual Fellowship (European Commission) (MCIF: No. 745776). The research data underpinning this publication can be accessed at https://doi.org/10.17630/4b1c9e3d-7787-40c8-aade-1dcf1af62315

References:

(1) Luo, D.; Su, R.; Zhang, W.; Gong, Q.; Zhu, R. Minimizing non-radiative recombination losses in perovskite solar cells. *Nature Reviews Materials* **2020,** *5* (1) 44-60.
(2) Saidaminov, M. I.; Kim, J.; Jain, A.; Quintero-Bermudez, R.; Tan, H.; Long, G.; Tan, F.; Johnston, A.; Zhao, Y.; Voznyy, O.; Sargent, E. H. Suppression of atomic vacancies via incorporation of isovalent small ions to increase the stability of halide perovskite solar cells in ambient air. *Nature Energy* **2018,** *3* (8) 648-654.
(3) Aydin, E.; De Bastiani, M.; De Wolf, S. Defect and Contact Passivation for Perovskite Solar Cells. *Advanced Materials* **2019,** *31* (25) 1900428.
(4) Tennyson, E. M.; Doherty, T. A. S.; Stranks, S. D. Heterogeneity at multiple length scales in halide perovskite semiconductors. *Nature Reviews Materials* **2019,** *4* (9) 573-587.
(5) Li, X.; Luo, Y.; Holt, M. V.; Cai, Z.; Fenning, D. P. Residual Nanoscale Strain in Cesium Lead Bromide Perovskite Reduces Stability and Shifts Local Luminescence. *Chemistry of Materials* **2019,** *31* (8) 2778-2785.
(6) Zhao, J.; Deng, Y.; Wei, H.; Zheng, X.; Yu, Z.; Shao, Y.; Shield, J. E.; Huang, J. Strained hybrid perovskite thin films and their impact on the intrinsic stability of perovskite solar cells. *Science Advances* **2017,** *3* (11) eaao5616.
(7) Jones, T. W.; Osherov, A.; Alsari, M.; Sponseller, M.; Duck, B. C.; Jung, Y.-K.; Settens, C.; Niroui, F.; Brenes, R.; Stan, C. V.; Li, Y.; Abdi-Jalebi, M.; Tamura, N.; Macdonald, J. E.; Burghammer, M.; Friend, R. H.; Bulović, V.; Walsh, A.; Wilson, G. J.; Lilliu, S.; Stranks, S.

D. Lattice strain causes non-radiative losses in halide perovskites. *Energy & Environmental Science* **2019,** *12* (2) 596-606.
(8) Nishida, J.; Alfaifi, A. H.; Gray, T. P.; Shaheen, S. E.; Raschke, M. B. Heterogeneous Cation–Lattice Interaction and Dynamics in Triple-Cation Perovskites Revealed by Infrared Vibrational Nanoscopy. *ACS Energy Letters* **2020,** 1636-1643.
(9) Jin, H.; Debroye, E.; Keshavarz, M.; Scheblykin, I. G.; Roeffaers, M. B. J.; Hofkens, J.; Steele, J. A. It's a trap! On the nature of localised states and charge trapping in lead halide perovskites. *Materials Horizons* **2020,** *7* (2) 397-410.
(10) de Quilettes, D. W.; Vorpahl, S. M.; Stranks, S. D.; Nagaoka, H.; Eperon, G. E.; Ziffer, M. E.; Snaith, H. J.; Ginger, D. S. Impact of microstructure on local carrier lifetime in perovskite solar cells. *Science* **2015,** *348* (6235) 683-686.
(11) deQuilettes, D. W.; Zhang, W.; Burlakov, V. M.; Graham, D. J.; Leijtens, T.; Osherov, A.; Bulović, V.; Snaith, H. J.; Ginger, D. S.; Stranks, S. D. Photo-induced halide redistribution in organic–inorganic perovskite films. *Nature Communications* **2016,** *7* (1) 11683.
(12) deQuilettes, D. W.; Jariwala, S.; Burke, S.; Ziffer, M. E.; Wang, J. T. W.; Snaith, H. J.; Ginger, D. S. Tracking Photoexcited Carriers in Hybrid Perovskite Semiconductors: Trap-Dominated Spatial Heterogeneity and Diffusion. *ACS Nano* **2017,** *11* (11) 11488-11496.
(13) deQuilettes, D. W.; Koch, S.; Burke, S.; Paranji, R. K.; Shropshire, A. J.; Ziffer, M. E.; Ginger, D. S. Photoluminescence Lifetimes Exceeding 8 μs and Quantum Yields Exceeding 30% in Hybrid Perovskite Thin Films by Ligand Passivation. *ACS Energy Letters* **2016,** *1* (2) 438-444.
(14) Doherty, T. A. S.; Winchester, A. J.; Macpherson, S.; Johnstone, D. N.; Pareek, V.; Tennyson, E. M.; Kosar, S.; Kosasih, F. U.; Anaya, M.; Abdi-Jalebi, M.; Andaji-Garmaroudi, Z.; Wong, E. L.; Madéo, J.; Chiang, Y.-H.; Park, J.-S.; Jung, Y.-K.; Petoukhoff, C. E.; Divitini, G.; Man, M. K. L.; Ducati, C.; Walsh, A.; Midgley, P. A.; Dani, K. M.; Stranks, S. D. Performance-limiting nanoscale trap clusters at grain junctions in halide perovskites. *Nature* **2020,** *580* (7803) 360-366.
(15) Bischak, C. G.; Sanehira, E. M.; Precht, J. T.; Luther, J. M.; Ginsberg, N. S. Heterogeneous Charge Carrier Dynamics in Organic–Inorganic Hybrid Materials: Nanoscale Lateral and Depth-Dependent Variation of Recombination Rates in Methylammonium Lead Halide Perovskite Thin Films. *Nano Letters* **2015,** *15* (7) 4799-4807.
(16) Bischak, C. G.; Hetherington, C. L.; Wu, H.; Aloni, S.; Ogletree, D. F.; Limmer, D. T.; Ginsberg, N. S. Origin of Reversible Photoinduced Phase Separation in Hybrid Perovskites. *Nano Letters* **2017,** *17* (2) 1028-1033.
(17) Dar, M. I.; Hinderhofer, A.; Jacopin, G.; Belova, V.; Arora, N.; Zakeeruddin, S. M.; Schreiber, F.; Grätzel, M. Function Follows Form: Correlation between the Growth and Local Emission of Perovskite Structures and the Performance of Solar Cells. *Advanced Functional Materials* **2017,** *27* (26) 1701433.
(18) Guthrey, H.; Moseley, J. A Review and Perspective on Cathodoluminescence Analysis of Halide Perovskites. *Advanced Energy Materials* **2020** 1903840.
(19) Su, T.-S.; Eickemeyer, F. T.; Hope, M. A.; Jahanbakhshi, F.; Mladenović, M.; Li, J.; Zhou, Z.; Mishra, A.; Yum, J.-H.; Ren, D.; Krishna, A.; Ouellette, O.; Wei, T.-C.; Zhou, H.; Huang, H.-H.; Mensi, M. D.; Sivula, K.; Zakeeruddin, S. M.; Milić, J. V.; Hagfeldt, A.; Rothlisberger, U.; Emsley, L.; Zhang, H.; Grätzel, M. Crown Ether Modulation Enables over 23% Efficient Formamidinium-Based Perovskite Solar Cells. *Journal of the American Chemical Society* **2020,** *142* (47) 19980-19991.
(20) Li, S.; Ding, H.; Cai, H.; Zhao, H.; Zhao, Y.; Yang, J.; Jin, Y.; Pan, N.; Wang, X. Realizing CsPbBr3 Light-Emitting Diode Arrays Based on PDMS Template Confined

Solution Growth of Single-Crystalline Perovskite. *The Journal of Physical Chemistry Letters* **2020,** *11* (19) 8275-8282.

(21) Wang, X.; Chen, H.; Zhou, H.; Wang, X.; Yuan, S.; Yang, Z.; Zhu, X.; Ma, R.; Pan, A. Room-temperature high-performance CsPbBr3 perovskite tetrahedral microlasers. *Nanoscale* **2019,** *11* (5) 2393-2400.

(22) Jaysankar, M.; Raul, B. A. L.; Bastos, J.; Burgess, C.; Weijtens, C.; Creatore, M.; Aernouts, T.; Kuang, Y. H.; Gehlhaar, R.; Hadipour, A.; Poortmans, J. Minimizing Voltage Loss in Wide-Bandgap Perovskites for Tandem Solar Cells. *Acs Energy Letters* **2019,** *4* (1) 259-264.

(23) Yuan, L.; Wang, Z.; Duan, R.; Huang, P.; Zhang, K.; Chen, Q.; Allam, N. K.; Zhou, Y.; Song, B.; Li, Y. Semi-transparent perovskite solar cells: unveiling the trade-off between transparency and efficiency. *Journal of Materials Chemistry A* **2018,** *6* (40) 19696-19702.

(24) Mathews, I.; Kantareddy, S. N. R.; Sun, S.; Layurova, M.; Thapa, J.; Correa-Baena, J.-P.; Bhattacharyya, R.; Buonassisi, T.; Sarma, S.; Peters, I. M. Self-Powered Sensors Enabled by Wide-Bandgap Perovskite Indoor Photovoltaic Cells. *Advanced Functional Materials* **2019,** *29* (42) 1904072.

(25) Li, X.; Tan, Y.; Lai, H.; Li, S.; Chen, Y.; Li, S.; Xu, P.; Yang, J. All-Inorganic CsPbBr3 Perovskite Solar Cells with 10.45% Efficiency by Evaporation-Assisted Deposition and Setting Intermediate Energy Levels. *ACS Applied Materials & Interfaces* **2019,** *11* (33) 29746-29752.

(26) Liu, Z.; Hu, Z.; Shi, T.; Du, J.; Yang, J.; Zhang, Z.; Tang, X.; Leng, Y. Stable and enhanced frequency up-converted lasing from CsPbBr3 quantum dots embedded in silica sphere. *Opt. Express* **2019,** *27* (7) 9459-9466.

(27) Zeng, J.; Meng, C.; Li, X.; Wu, Y.; Liu, S.; Zhou, H.; Wang, H.; Zeng, H. Interfacial-Tunneling-Effect-Enhanced CsPbBr3 Photodetectors Featuring High Detectivity and Stability. *Advanced Functional Materials* **2019,** *29* (51) 1904461.

(28) Kulbak, M.; Gupta, S.; Kedem, N.; Levine, I.; Bendikov, T.; Hodes, G.; Cahen, D. Cesium Enhances Long-Term Stability of Lead Bromide Perovskite-Based Solar Cells. *The Journal of Physical Chemistry Letters* **2016,** *7* (1) 167-172.

(29) Zohar, A.; Kulbak, M.; Levine, I.; Hodes, G.; Kahn, A.; Cahen, D. What Limits the Open-Circuit Voltage of Bromide Perovskite-Based Solar Cells? *ACS Energy Letters* **2019,** *4* (1) 1-7.

(30) Rudd, P. N.; Huang, J. Metal Ions in Halide Perovskite Materials and Devices. *Trends in Chemistry* **2019,** *1* (4) 394-409.

(31) Abdi-Jalebi, M.; Andaji-Garmaroudi, Z.; Pearson, A. J.; Divitini, G.; Cacovich, S.; Philippe, B.; Rensmo, H.; Ducati, C.; Friend, R. H.; Stranks, S. D. Potassium- and Rubidium-Passivated Alloyed Perovskite Films: Optoelectronic Properties and Moisture Stability. *ACS Energy Letters* **2018,** *3* (11) 2671-2678.

(32) Nam, J. K.; Chai, S. U.; Cha, W.; Choi, Y. J.; Kim, W.; Jung, M. S.; Kwon, J.; Kim, D.; Park, J. H. Potassium Incorporation for Enhanced Performance and Stability of Fully Inorganic Cesium Lead Halide Perovskite Solar Cells. *Nano Letters* **2017,** *17* (3) 2028-2033.

(33) Li, Y.; Duan, J.; Yuan, H.; Zhao, Y.; He, B.; Tang, Q. Lattice Modulation of Alkali Metal Cations Doped Cs1−xRxPbBr3 Halides for Inorganic Perovskite Solar Cells. *Solar RRL* **2018,** *2* (10) 1800164.

(34) Abdi-Jalebi, M.; Andaji-Garmaroudi, Z.; Cacovich, S.; Stavrakas, C.; Philippe, B.; Richter, J. M.; Alsari, M.; Booker, E. P.; Hutter, E. M.; Pearson, A. J.; Lilliu, S.; Savenije, T. J.; Rensmo, H.; Divitini, G.; Ducati, C.; Friend, R. H.; Stranks, S. D. Maximizing and stabilizing luminescence from halide perovskites with potassium passivation. *Nature* **2018,** *555* (7697) 497-501.

(35) Zhao, W.; Yao, Z.; Yu, F.; Yang, D.; Liu, S. Alkali Metal Doping for Improved CH3NH3PbI3 Perovskite Solar Cells. *Advanced Science* **2018,** *5* (2) 1700131.

(36) Bischak, C. G.; Lai, M.; Fan, Z.; Lu, D.; David, P.; Dong, D.; Chen, H.; Etman, A. S.; Lei, T.; Sun, J.; Grünwald, M.; Limmer, D. T.; Yang, P.; Ginsberg, N. S. Liquid-like Interfaces Mediate Structural Phase Transitions in Lead Halide Perovskites. *Matter* **2020,** *3* (2) 534-545.

(37) Li, W.; Rothmann, M. U.; Liu, A.; Wang, Z.; Zhang, Y.; Pascoe, A. R.; Lu, J.; Jiang, L.; Chen, Y.; Huang, F.; Peng, Y.; Bao, Q.; Etheridge, J.; Bach, U.; Cheng, Y.-B. Phase Segregation Enhanced Ion Movement in Efficient Inorganic CsPbIBr2 Solar Cells. *Advanced Energy Materials* **2017,** *7* (20) 1700946.

(38) Guthrey, H.; Moseley, J. A Review and Perspective on Cathodoluminescence Analysis of Halide Perovskites. *Advanced Energy Materials* **2020,** *10* (26) 1903840.

(39) Martin, R. W.; Edwards, P. R.; O'Donnell, K. P.; Dawson, M. D.; Jeon, C.-W.; Liu, C.; Rice, G. R.; Watson, I. M. Cathodoluminescence spectral mapping of III-nitride structures. *physica status solidi (a)* **2004,** *201* (4) 665-672.

(40) Edwards, P. R.; Martin, R. W. Cathodoluminescence nano-characterization of semiconductors. *Semiconductor Science and Technology* **2011,** *26* (6) 064005.

(41) Edwards, P. R.; Jagadamma, L. K.; Bruckbauer, J.; Liu, C.; Shields, P.; Allsopp, D.; Wang, T.; Martin, R. W. High-Resolution Cathodoluminescence Hyperspectral Imaging of Nitride Nanostructures. *Microscopy and Microanalysis* **2012,** *18* (6) 1212-1219.

(42) Li, C.; Han, C.; Zhang, Y.; Zang, Z.; Wang, M.; Tang, X.; Du, J. Enhanced photoresponse of self-powered perovskite photodetector based on ZnO nanoparticles decorated CsPbBr3 films. *Solar Energy Materials and Solar Cells* **2017,** *172* 341-346.

(43) Li, C.; Zang, Z.; Han, C.; Hu, Z.; Tang, X.; Du, J.; Leng, Y.; Sun, K. Highly compact CsPbBr3 perovskite thin films decorated by ZnO nanoparticles for enhanced random lasing. *Nano Energy* **2017,** *40* 195-202.

(44) Venkateswararao, A.; Ho, J. K. W.; So, S. K.; Liu, S.-W.; Wong, K.-T. Device characteristics and material developments of indoor photovoltaic devices. *Materials Science and Engineering: R: Reports* **2020,** *139* 100517.

(45) Lee, K.; Um, H.-D.; Choi, D.; Park, J.; Kim, N.; Kim, H.; Seo, K. The Development of Transparent Photovoltaics. *Cell Reports Physical Science* **2020,** *1* (8) 100143.

(46) El Ajjouri, Y.; Chirvony, V. S.; Sessolo, M.; Palazon, F.; Bolink, H. J. Incorporation of potassium halides in the mechanosynthesis of inorganic perovskites: feasibility and limitations of ion-replacement and trap passivation. *RSC Advances* **2018,** *8* (72) 41548-41551.

(47) Pathak, S.; Sakai, N.; Wisnivesky Rocca Rivarola, F.; Stranks, S. D.; Liu, J.; Eperon, G. E.; Ducati, C.; Wojciechowski, K.; Griffiths, J. T.; Haghighirad, A. A.; Pellaroque, A.; Friend, R. H.; Snaith, H. J. Perovskite Crystals for Tunable White Light Emission. *Chemistry of Materials* **2015,** *27* (23) 8066-8075.

(48) Brenner, P.; Glöckler, T.; Rueda-Delgado, D.; Abzieher, T.; Jakoby, M.; Richards, B. S.; Paetzold, U. W.; Howard, I. A.; Lemmer, U. Triple cation mixed-halide perovskites for tunable lasers. *Opt. Mater. Express* **2017,** *7* (11) 4082-4094.

(49) He, Y.; Matei, L.; Jung, H. J.; McCall, K. M.; Chen, M.; Stoumpos, C. C.; Liu, Z.; Peters, J. A.; Chung, D. Y.; Wessels, B. W.; Wasielewski, M. R.; Dravid, V. P.; Burger, A.; Kanatzidis, M. G. High spectral resolution of gamma-rays at room temperature by perovskite CsPbBr3 single crystals. *Nature Communications* **2018,** *9* (1) 1609.

(50) Bruzzi, M.; Gabelloni, F.; Calisi, N.; Caporali, S.; Vinattieri, A. Defective States in Micro-Crystalline $CsPbBr_3$ and Their Role on Photoconductivity. *Nanomaterials (Basel)* **2019,** *9* (2) 177.

(51) Zhang, H.; Liu, X.; Dong, J.; Yu, H.; Zhou, C.; Zhang, B.; Xu, Y.; Jie, W. Centimeter-Sized Inorganic Lead Halide Perovskite CsPbBr3 Crystals Grown by an Improved Solution Method. *Crystal Growth & Design* **2017,** *17* (12) 6426-6431.
(52) Senocrate, A.; Yang, T.-Y.; Gregori, G.; Kim, G. Y.; Grätzel, M.; Maier, J. Charge carrier chemistry in methylammonium lead iodide. *Solid State Ionics* **2018,** *321* 69-74.
(53) He, X.; Qiu, Y.; Yang, S. Fully-Inorganic Trihalide Perovskite Nanocrystals: A New Research Frontier of Optoelectronic Materials. *Advanced Materials* **2017,** *29* (32) 1700775.
(54) Zhou, Y.; Chen, J.; Bakr, O. M.; Sun, H.-T. Metal-Doped Lead Halide Perovskites: Synthesis, Properties, and Optoelectronic Applications. *Chemistry of Materials* **2018,** *30* (19) 6589-6613.
(55) ICDS 109295.
(56) Jariwala, S.; Sun, H.; Adhyaksa, G. W. P.; Lof, A.; Muscarella, L. A.; Ehrler, B.; Garnett, E. C.; Ginger, D. S. Local Crystal Misorientation Influences Non-radiative Recombination in Halide Perovskites. *Joule* **2019,** *3* (12) 3048-3060.
(57) Liu, Y.; Collins, L.; Proksch, R.; Kim, S.; Watson, B. R.; Doughty, B.; Calhoun, T. R.; Ahmadi, M.; Ievlev, A. V.; Jesse, S.; Retterer, S. T.; Belianinov, A.; Xiao, K.; Huang, J.; Sumpter, B. G.; Kalinin, S. V.; Hu, B.; Ovchinnikova, O. S. Chemical nature of ferroelastic twin domains in CH3NH3PbI3 perovskite. *Nature Materials* **2018,** *17* (11) 1013-1019.
(58) Rothmann, M. U.; Kim, J. S.; Borchert, J.; Lohmann, K. B.; O'Leary, C. M.; Sheader, A. A.; Clark, L.; Snaith, H. J.; Johnston, M. B.; Nellist, P. D.; Herz, L. M. Atomic-scale microstructure of metal halide perovskite. *Science* **2020,** *370* (6516) eabb5940.
(59) Petrov, V. I.; Gvozdover, R. S. Spatial resolution of cathodoluminescence scanning electron microscopy of semiconductors. *Scanning* **1991,** *13* (6) 410-414.
(60) Drouin, D.; Couture, A. R.; Joly, D.; Tastet, X.; Aimez, V.; Gauvin, R. CASINO V2.42—A Fast and Easy-to-use Modeling Tool for Scanning Electron Microscopy and Microanalysis Users. *Scanning* **2007,** *29* (3) 92-101.
(61) Diab, H.; Arnold, C.; Lédée, F.; Trippé-Allard, G.; Delport, G.; Vilar, C.; Bretenaker, F.; Barjon, J.; Lauret, J.-S.; Deleporte, E.; Garrot, D. Impact of Reabsorption on the Emission Spectra and Recombination Dynamics of Hybrid Perovskite Single Crystals. *The Journal of Physical Chemistry Letters* **2017,** *8* (13) 2977-2983.
(62) Brennan, M. C.; Draguta, S.; Kamat, P. V.; Kuno, M. Light-Induced Anion Phase Segregation in Mixed Halide Perovskites. *ACS Energy Letters* **2018,** *3* (1) 204-213.
(63) Mahesh, S.; Ball, J. M.; Oliver, R. D. J.; McMeekin, D. P.; Nayak, P. K.; Johnston, M. B.; Snaith, H. J. Revealing the origin of voltage loss in mixed-halide perovskite solar cells. *Energy & Environmental Science* **2020,** *13* (1) 258-267.
(64) Tong, G.; Ono, L. K.; Qi, Y. Recent Progress of All-Bromide Inorganic Perovskite Solar Cells. *Energy Technology* **2020,** *8* (4) 1900961.
(65) Unger, E. L.; Kegelmann, L.; Suchan, K.; Sörell, D.; Korte, L.; Albrecht, S. Roadmap and roadblocks for the band gap tunability of metal halide perovskites. *Journal of Materials Chemistry A* **2017,** *5* (23) 11401-11409.
(66) Jiang, L.; Fang, Z.; Lou, H.; Lin, C.; Chen, Z.; Li, J.; He, H.; Ye, Z. Achieving long carrier lifetime and high optical gain in all-inorganic CsPbBr3 perovskite films via top and bottom surface modification. *Physical Chemistry Chemical Physics* **2019,** *21* (39) 21996-22001.
(67) Wang, D.; Liu, R. Q.; Tan, X.; Liu, Q.; Nan, H. R.; Sang, S. L.; Chen, F.; Huang, W. Amplified spontaneous emission properties of solution processed CsPbBr3 perovskite thin films doped with large-group ammonium cations. *Optical Materials Express* **2020,** *10* (4) 981-997.
(68) Wang, R.; Jia, Y.-L.; Ding, L.; He, Z.; Dong, Y.; Ma, X.-J.; Zhang, Y.; Zhou, D.-Y.; Zhu, Z.-X.; Xiong, Z.-H.; Gao, C.-H. Efficient halide perovskite light-emitting diodes with

emissive layer consisted of multilayer coatings. *Journal of Applied Physics* **2019,** *126* (16) 165502.
(69) Habisreutinger, S. N.; Noel, N. K.; Snaith, H. J. Hysteresis Index: A Figure without Merit for Quantifying Hysteresis in Perovskite Solar Cells. *ACS Energy Letters* **2018,** *3* (10) 2472-2476.
(70) Stranks, S. D.; Hoye, R. L. Z.; Di, D.; Friend, R. H.; Deschler, F. The Physics of Light Emission in Halide Perovskite Devices. *Advanced Materials* **2019,** *31* (47) 1803336.

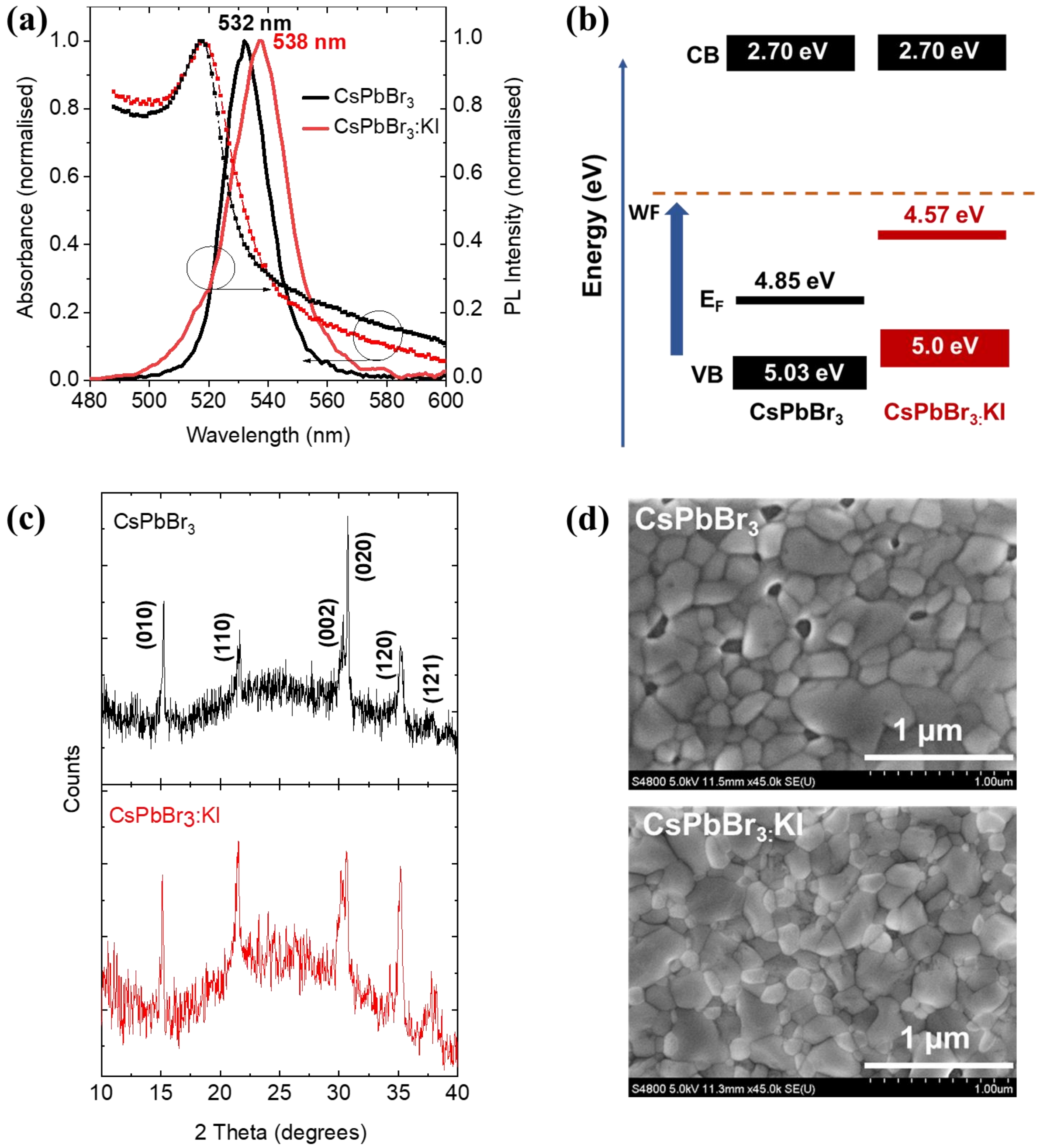

Figure 1(a) The UV-vis absorption and photoluminescence (PL) spectra of the $CsPbBr_3$ and $CsPbBr_3$:KI films. The PL excitation wavelength is 400 nm. (b) The electronic band structure of the $CsPbBr_3$ and $CsPbBr_3$:KI films obtained using Kelvin probe and ambient photoemission spectroscopy. (c) The X-ray diffraction patterns of the $CsPbBr_3$ and $CsPbBr_3$:KI films. (d) The surface morphology of the $CsPbBr_3$ and $CsPbBr_3$:KI films imaged using scanning electron microscopy. The vertical scaling has not been corrected for the 45° sample tilt. In-plane distances in the vertical dimension should be multiplied by ~1.4 to account for this

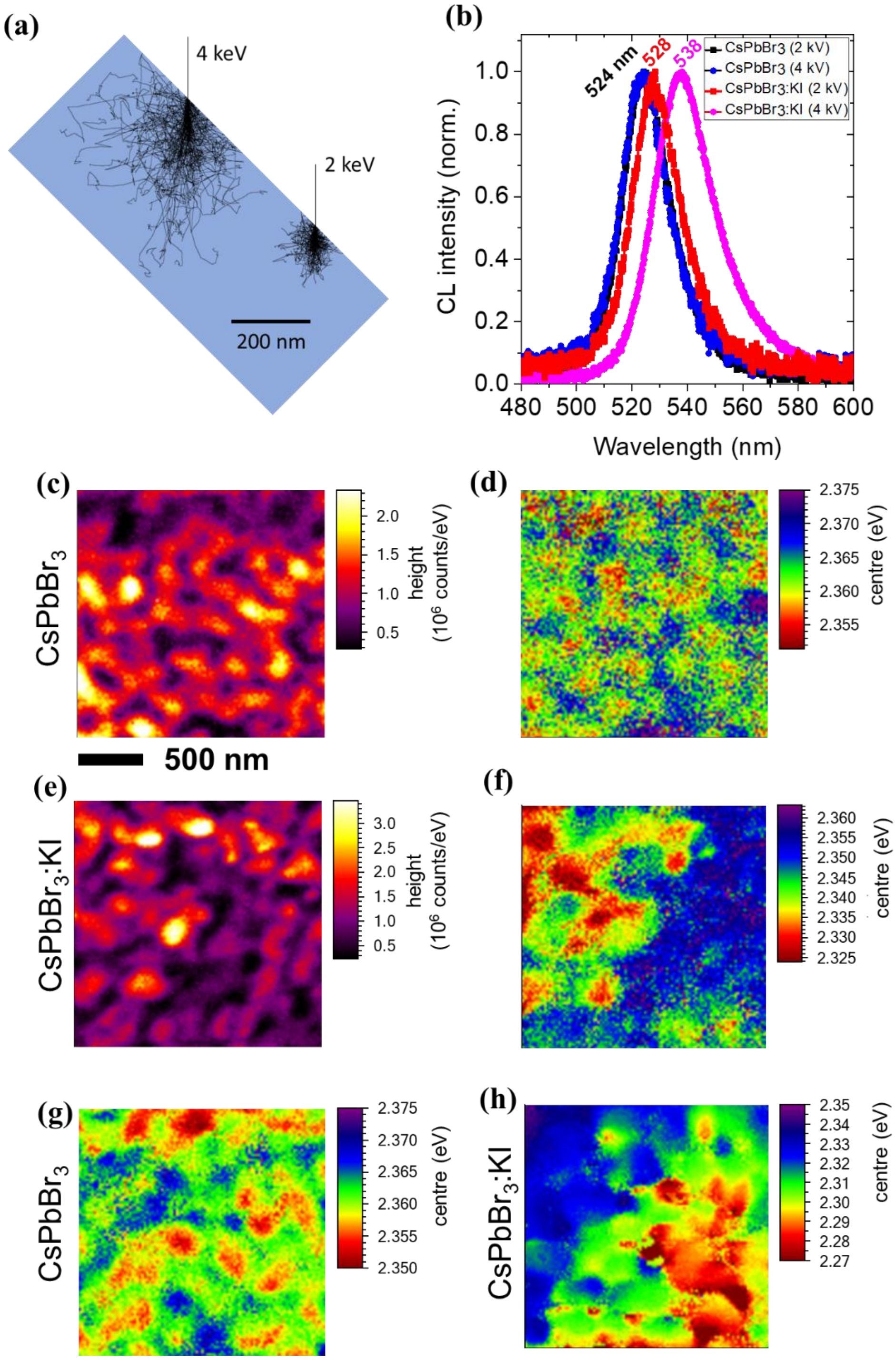

Figure 2: (a) Monte-Carlo simulation showing the electron trajectories in the $CsPbBr_3$ thin film sample of thickness 200 nm under electron beam acceleration voltages of 2 and 4 kV. (b) Depth resolved CL spectra from the $CsPbBr_3$ and $CsPbBr_3$:KI thin film samples. 2D spatial maps of (c) peak intensity and (d) peak emission energy of the CL emission from $CsPbBr_3$ at 2kV. 2D spatial maps of (e) peak intensity and (f) peak emission energy of the CL emission from $CsPbBr_3$:KI at 2kV. 2D spatial map of (g) peak emission energy for $CsPbBr_3$ at 4 kV. 2D spatial map of (h) peak emission energy for $CsPbBr_3$:KI at 4 kV. The vertical scaling has not been corrected for the 45° sample tilt. In-plane distances in the vertical dimension should be multiplied by ~1.4 to account for this

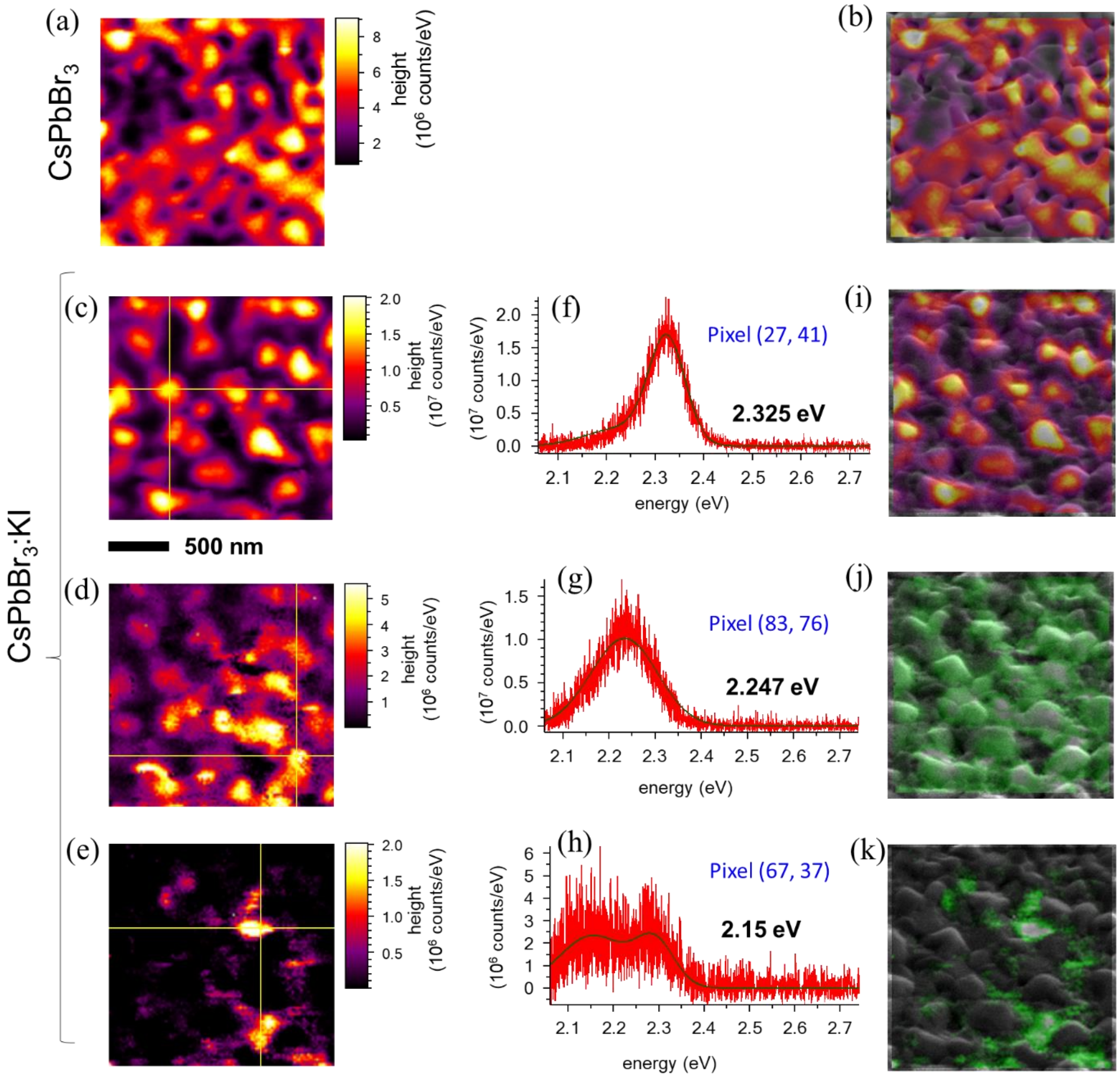

Figure 3: 2D spatial maps of **(a)** peak intensity of the CL emission from $CsPbBr_3$ obtained using a 4 kV electron beam voltage. The overlaying of the corresponding map on the secondary electron topographic image is shown in Figure 3**(b)**. **(c–e)** Fitted peak intensity maps corresponding to three different components of the emission from the $CsPbBr_3$:KI sample under 4 kV beam excitation. The representative fitted CL emission spectra are shown in **(f–h)**. The overlaid intensity maps on the SE images for these CL emission components are shown in **(i–k)**. The vertical scaling has not been corrected for the 45° sample tilt. In-plane distances in the vertical dimension should be multiplied by ~1.4 to account for this. The corresponding SE image is shown in Figure S6(b).

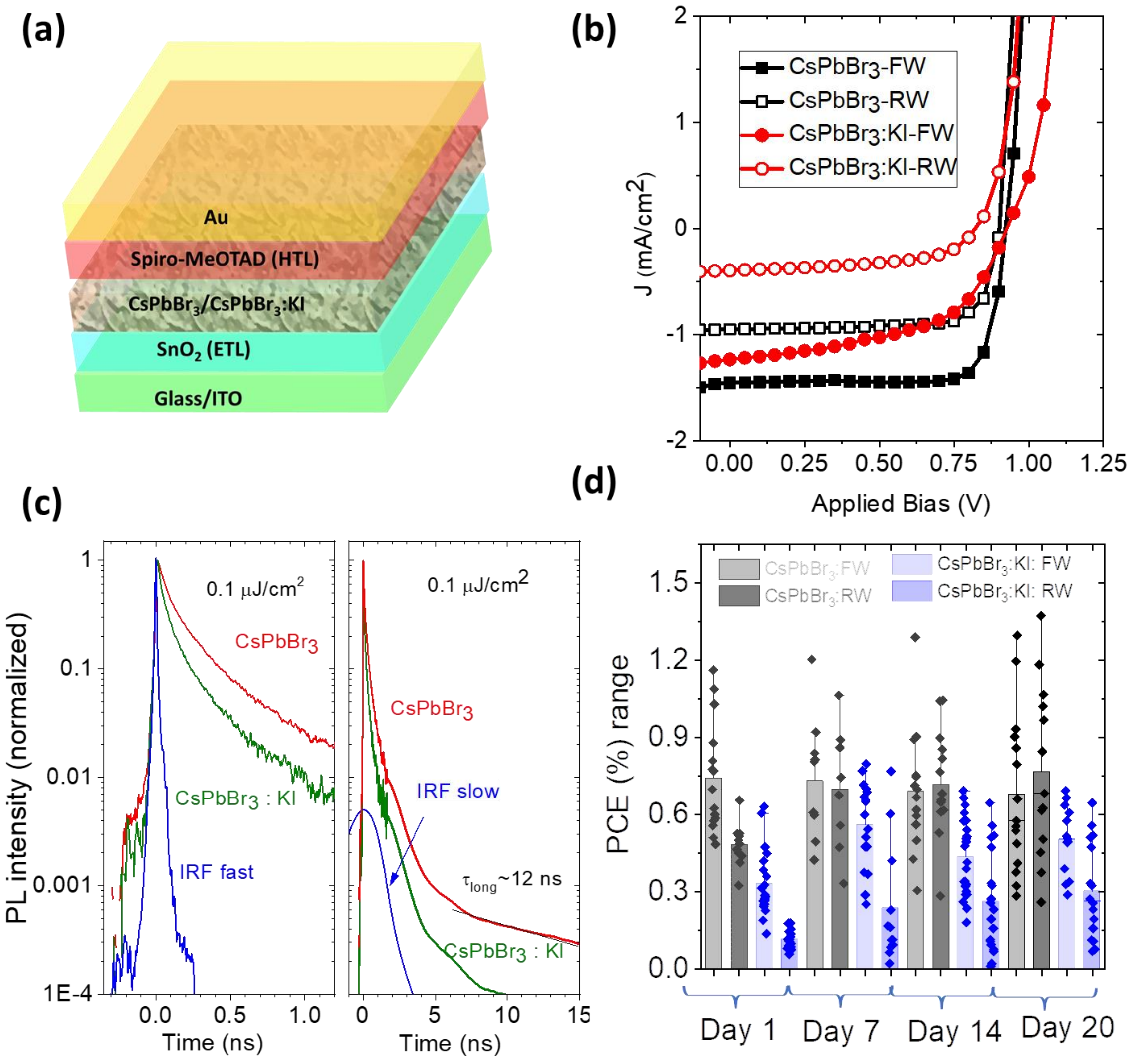

Figure 4: **(a)** The n-i-p device architecture used for the fabrication. **(b)** Current-voltage characteristics of the $CsPbBr_3$ and $CsPbBr_3$:KI based solar cells. FW stands for the forward scan and RW stands for the reverse scan. **(c)** Photoluminescence decays on a short (left) and long (right) time scales and the instrument response functions (IRF) of the fast and slow streak cameras. (d) Shelf-life stability study showing the variation of power conversion efficiency of the fabricated devices over a period of 20 days.

Table of Contents (TOC) graphic